AIAA

A01-16413

AIAA-2001-0541
Aircraft Flight Dynamics with Simulated Ice Accretion
D. Pokhariyal, M.B. Bragg, T. Hutchison, and J. Merret
University of Illinois at Urbana-Champaign
Urbana, Illinois

39th AIAA Aerospace Sciences Meeting & Exhibit
8-11 January 2001 / Reno, NV

Aircraft Flight Dynamics with Simulated Ice Accretion

Devesh Pokhariyal,[+] Michael B. Bragg,[†] Tim Hutchison,[^] and Jason Merret[*]

University of Illinois at Urbana-Champaign

ABSTRACT

The effect of ice accretion on aircraft performance and control during trim conditions was modeled and analyzed. A six degree-of-freedom computational flight dynamics model was used to study the effect of ice accretion on the aircraft dynamics. The effects of turbulence and sensor noise were modeled and filters were developed to remove unwanted noisy data without affecting the short period and phugoid modes. This study is part of a larger research program to develop smart icing system technology. The goal of the study reported here was to develop techniques to sense the effect and location of ice accretion on aircraft performance and control during trimmed flight. Control surface steady and unsteady hinge-moments were modeled as a potential aerodynamic performance sensor. Microburst and gravity wave atmospheric disturbances were modeled and their effects on the aircraft performance and control were compared to that of an icing encounter. The simulations showed that atmospheric disturbances could be differentiated from icing encounters. The hinge-moment sensors proved very useful in identifying the wing versus tail location of aircraft icing.

LIST OF SYMBOLS AND ABBREVIATIONS

$C_{(A)}$	arbitrary performance or stability and control derivative
C_d	airfoil drag coefficient
C_h	hinge-moment coefficient
$C_{h,\,RMS}$	unsteady hinge-moment coefficient
C_ℓ	lift coefficient
Cm	pitching moment coefficient
F_x, F_y, F_z	forces on the aircraft
FDC	Flight Dynamics Code
g(n)	freezing fraction effect on drag
h	altitude
IMS	Ice Management System
IPS	Icing Protection System
k_{C_A}	coefficient icing factor constant
k'_{C_A}	coefficient icing factor
LWC	Liquid Water Content
MVD	Median Volumetric Diameter
m	aircraft mass
n	freezing fraction
p, q, r	aircraft angular velocities
q_g	effective pitch rate due to gust velocity
r	radial coordinate
R	microburst radius
SIS	Smart Icing System
T	temperature
t	time
TIP	Tailplane Icing Program
u, v, w	atmospheric velocities
V	aircraft, freestream velocity
x, y, z	rectangular coordinates
$Z_{1,2,3}$	drag equation constants
z*	characteristic height out of the boundary layer
Δ	change
α	angle of attack
δ_e	elevator deflection
λ	microburst constant
η	aircraft icing parameter
η_{ice}	icing severity parameter

[+] Graduate Research Assistant, Department of Aeronautical and Astronautical Engineering, currently Aerospace/Simulation Engineer, NLX Corporation, Sterling, VA, Member AIAA.
[†] Professor and Head, Department of Aeronautical and Astronautical Engineering, Associate Fellow AIAA.
[^] Graduate Research Assistant, Department of Aeronautical and Astronautical Engineering, currently Aeronautical Engineer, Naval Air Warfare Center – Aircraft Division, Patuxent River, MD, Member AIAA.
[*] Graduate Research Assistant, Department of Aeronautical and Astronautical Engineering, Member AIAA.

1.0 INTRODUCTION

The research presented in this paper was a continuation of the work presented by Bragg et al.[1] Recent commuter aircraft icing accidents highlight the need for improved safety. The primary cause of these accidents was the effect of ice on aircraft control.[2] With a projected growth in airline traffic, the need to address aircraft icing and its effects on aircraft handling qualities is apparent. As mentioned by Bragg et al.,[1] icing accidents can be prevented in two different ways: 1) icing conditions can be avoided, or 2) the aircraft system can be designed and operated in an ice tolerant manner. For all aircraft, ice avoidance is a desirable goal for increased safety. However, for commercial aircraft, where revenue and schedules must be maintained, ice tolerance will continue to be the preferred method for all but the most severe icing conditions. Our approach is to conduct research to improve the safety of operations in icing conditions (ice tolerance) by developing the Smart Icing Systems (SIS) concept.

In this paper, a simple model is presented to include the effect of ice on linear and nonlinear aircraft stability and control derivatives. A more accurate model based on a neural network approach is also discussed. This technique is used in conjunction with a six degree-of-freedom computational flight mechanics model to study the effects of ice on aircraft dynamics. Control surface hinge-moments are evaluated for possible use in detecting the effect and location of ice accretion in flight when insufficient dynamic content, such as the vehicle response to an elevator doublet, is available to use system identification techniques. Much research has been conducted to determine the effect of ice on performance and handling qualities, however other phenomena, such as atmospheric disturbance can potentially cause similar effects. Research is presented here on aircraft microburst and gravity wave encounters to understand how those can be identified to eliminate false alarms.

2.0 THEORETICAL AND COMPUTATIONAL METHODS

2.1 Iced Aircraft Model Development

A simple, but physically representative, model of the effect of ice on aircraft flight mechanics is used in this paper. The method was described in detail in a previous paper[1] and will only be reviewed here and some recent improvements presented. The icing effects model is based on the following equation

$$C_{(A)iced} = (1 + \eta_{ice} k'_{C_A})C_{(A)}$$

In this equation, η_{ice} is an icing severity parameter, and represents the amount and severity of the icing encounter. η_{ice} is defined such that it is not a function of the aircraft, only the atmospheric conditions. k'_{C_A} is the coefficient icing factor that depends the coefficient being modified and the aircraft specific information. Here the k'_{C_A} term accounts for one aircraft due to its size, speed, or design being more susceptible to icing than another aircraft. $C_{(A)}$ is any arbitrary performance, stability or control parameter or derivative that is affected by ice accretion.

In this formulation, the weighting factor, k'_{C_A}, is assumed to be

$$k'_{C_A} = \frac{\eta}{\eta_{ice}} k_{C_A}$$

Here the term η_{ice} is the ratio of the drag rise on a NACA 0012 airfoil at the current icing cloud conditions to the drag rise experienced at a reference condition in the continuous maximum icing envelope. The equation for η_{ice} is

$$\eta_{ice} = \frac{\Delta C_d (NACA\ 0012, c = 3', V = 175kts, actual.conditions)}{\Delta C_{d_{ref}} (NACA\ 0012, c = 3', cont.\ max.conditions)}$$

The η_{ice} value is calculated as above, using a three-foot chord NACA 0012 airfoil at 175 knots. Here η, the aircraft icing parameter, is calculated in the same way as η_{ice} except the chord and velocity corresponding the aircraft and conditions being examined are used in the numerator. The k_{C_A} represents the change in an aircraft parameter C_A, that is constant for a given aircraft. By using this formulation, the aircraft specific chord, airfoil, and velocity are adequately captured, allowing for a more accurate determination of iced coefficient values.

Recently the iced aircraft model has undergone some minor refinements. The database of icing cases used to define the model was expanded to include 115 distinct icing cases that were extracted from data taken at the NASA Lewis Icing Research Tunnel and presented in three separate NASA Technical Memorandums.[3-5] Approximately 86% of these cases were based on the NACA 0012 airfoil, and the remaining 14% were based on the NACA 63(2)-A415 airfoil.

The equation for the ΔC_d curves has the following general form for t < 10 minutes:

$$\Delta C_d = Z_1 \cdot (A_c E) \cdot g(n)$$

Where Z_1 is a constant, and the function g varies in a nonlinear fashion with n, peaking at a value of 0.2. As before, the ΔC_d curves were constructed to vary linearly with the value of $A_c E$ (and time) until the time of the encounter reached 10 minutes. Once the length of the icing encounter exceeded ten minutes, a linear variation with time was no longer representative of the actual drag increase. Since approximately only 10% of the cases in the database provided data for encounters beyond ten minutes, the formulation for long time encounters was estimated. Once beyond the ten minute threshold, the ΔC_d increase was estimated to decay exponentially to a point that was twice the ΔC_d value at ten minutes. The general form of the ΔC_d equation for t > 10 minutes was as follows:

$$\Delta C_d = Z_2 \cdot \left(1 - e^{Z_3\, t_{10}}\right) + \Delta C_{d\,(at\ 10\ minutes)}$$

Where Z_2 and Z_3 are constants based in part on the calculated value of ΔC_d at ten minutes, and t_{10} is the time elapsed after the passage of the ten-minute mark.

2.2 Neural Net Development

The correlations between atmospheric conditions, ice shapes and aircraft stability and control derivatives are very complex. In an attempt to develop an initial relationship between ice shapes and aerodynamic coefficients, neural networks have been implemented on recent experimental data to determine if a relationship could be found.

An excellent definition of a neural network was given by Haykin.[6] "A neural network is a massively parallel distributed processor made up of simple processing units, which has a natural propensity for storing experiential knowledge and making it available for use." Neural networks are loosely based on the structure of the human brain. Figure 1 is a schematic diagram of a neural network with four inputs and four outputs. There are several hidden layers of interconnected nodes within the neural network that take the provided inputs, multiply them by "synaptic weights," and then output the results either to another hidden layer or the output layer. The values of the synaptic weights are determined by training the neural network with known correlations. The synaptic weights of the nodes in a neural network can be linear or

nonlinear, and as such, neural networks are excellent in handling nonlinear data. There are many different applications for neural networks, one of which is finding correlations within complex sets of data. In this research, neural networks have been used in this manner as a powerful curve-fitting tool, attempting to correlate the characteristics of ice shapes to aerodynamic variables.

The data used for this exploration were taken from a paper by Kim and Bragg.[7] These data provide the C_l, C_d, C_m and C_h for a NLF-0414 airfoil with three different simulated glaze ice horn heights and six different locations over a range of angles of attack. The data also contain the effect of three different horn base widths and three different horn leading-edge radii. The variations of these values resulted in a database of 1,740 separate data points.

Using the Matlab Neural Network Toolbox, different neural nets were created using the 1,740 data points. During the training, the neural network looks at each data point individually, and attempts to adjust the synaptic weight of each node such that the inputs result in an output that is close to the known data. Each analysis of the entire data set is referred to as an epoch. For these networks, the Neural Network Toolbox was programmed to stop training after 500 epochs. Generally, the largest reduction in the error of the network occurs well before the first 150 epochs, after which there is very little increase in the accuracy of the network. This behavior is common when using neural nets to find trends in data, although the number of epochs to reach a reduction in error can vary significantly.

Each network consisted of five input nodes (angle of attack, horn location, horn height, horn base width and horn leading edge radius) and four output nodes (C_l, C_m, C_d and C_h). Several nets were trained, seeking the optimum configuration of hidden layers and nodes that provided the best correlation between experimental and "simulated" (within the neural net) data. Due to the large amount of data and epochs, training the neural nets took several hours on a 450 MHz Pentium-class processor, and as such, the training time was considered when choosing a network for the simulations. The current network being used in the simulations consist of five hidden layers of ten nodes each.

Initially, the neural networks were trained using all of the available data to determine if a correlation could be found between the ice shape parameters and aerodynamic coefficients. Once it was determined that a correlation existed, it was required to determine whether the neural net was able to predict values that were not in its training set. To this end, the neural nets were then retrained using only half of the available

data. This allows for a direct comparison between the network's simulated data and the unused experimental data.

Using the neural networks to determine the possible relationships between ice shapes and aerodynamic performance was only an initial step in a proposed chain of neural networks. Future research will test and develop two other sets of neural networks. One set would predict ice shapes based on the icing cloud parameters and aircraft information, while the other set would determine three-dimensional aerodynamic coefficients based on the two-dimensional coefficients. Combined with the neural networks described in this paper, these two additional sets would allow for a series of neural networks that would be able to relate environmental ice accretion parameters to three-dimensional aerodynamic coefficients and stability and control derivatives.

2.3 Clean and Iced Aircraft Models

The current longitudinal and lateral aircraft flight dynamics model was obtained from published NASA Twin Otter flight results. The results obtained from the Twin Otter flight with simulated tailplane icing were used to estimate most of the derivatives.[8,9] The drag and other non-tail related derivatives were obtained from flight test results in which the entire aircraft was subjected to icing.[10] Where values were not available, they were estimated. A comparison of the clean and iced derivatives is shown in Table 1. Also shown is a simple model of horizontal tail icing only and wing icing only, derived from these same data. The derivatives are representative of icing conditions that yield $\eta = 0.0675$. This model was intended primarily for use in the trimmed flight analysis performed in this paper.

2.4 Flight Mechanics Code

The flight analysis of the clean and iced aircraft models were carried out using the Flight Dynamics and Control (FDC) toolbox for MATLAB & Simulink.[11] The FDC code solves 12-coupled nonlinear differential equations to describe the aircraft's dynamic motion using control surface deflections, power, etc. as inputs. The FDC also incorporates an atmospheric turbulence model based on the NASA Dryden wind gust model. The onset and accumulation of icing are modeled during flight in the FDC code by modifying the aerodynamic derivatives at each time step as described by Bragg et al.[1] Various flight models can be incorporated into the FDC code and used to simulate

aircraft dynamics. The FDC code is modified as required and simulations are carried out in the open loop and autopilot modes. The code has also been updated to include sensor noise, microbursts and aerodynamic hinge-moment calculations.

A validation of the FDC code was carried out, by Bragg et al.,[1] where results obtained using the FDC were compared to those obtained by the method of Miller and Ribbens[12] and the NASA TIP flight p5220.

The effects of turbulence and sensor noise were incorporated into the FDC code as described in the paper by Bragg et.al.[1] Filters to remove unwanted noisy data without affecting the short period and phugoid modes were also developed.[1]

2.5 Hinge-Moment Measurements

Ice accretion on surfaces such as the leading edges of the wing and tail have a direct influence on the lift generation and the controllability of an aircraft. The effect of such ice build-up requires different recovery methods as shown by Ratvasky et al.[13] Non-uniform aircraft icing can result due to non uniform shedding as well as selective ice protection operation, or a failure. The many control related aircraft icing accidents highlight the importance of identifying icing-related control problems. The formation of ice on airfoil surfaces often results in a separation bubble, which severely alters the surface pressure distribution. On-board hinge-moment sensors were explored as a means to determine the effects of icing on different aircraft control surfaces.

Gurbacki and Bragg[14] measured hinge-moment, C_h, and unsteady hinge-moments, $C_{h,RMS}$, on a NACA 23012 airfoil with a flap. Data were collected for forward facing quarter round ice shapes placed at different x/c locations while varying the angle of attack and flap deflection. The hinge-moment measurements and the fluctuation of the hinge-moment (the unsteady rms value) capture the effects of icing on the flow field over the airfoil surface.

The results from Gurbacki and Bragg[14] showed that the hinge-moment measurements displayed trends that can be used to predict flow separation at angles of attack well before stall. Hinge-moment measurements can also be used to determine the location of ice accretion and the possible control degradation that can result.

A simple correlation between location of the quarter-round shape and the icing severity coefficient, η was used to quantify the effect of ice on the hinge-moment and the unsteady hinge-moment values. A hinge-moment and unsteady hinge-moment model was

created and incorporated into the FDC code. The effects of flap deflection were also modeled and can be used to represent the effect of any control surface deflection. The models are functions of angle of attack, control surface deflection and η. Details of these models can be found in Pokhariyal.[15]

These models accurately represent the hinge-moment behavior of the NACA 23012 airfoil, and are assumed to be representative of trends displayed by other airfoils. Figures 2 and 3 show the trends and variation of C_h and C_{hrms} models, respectively, as a function of angle of attack, η, and the control surface deflection. The models are compared to the experimental data for the NACA 23012.

Since the wing and tail surfaces were of different chord lengths, the η values used were based on the chord lengths of the respective surfaces. The η values used for the tail were based on the Twin Otter horizontal tail chord length of 4.75 ft, while the η values used for the wing were based on the Twin Otter wing chord length of 6.0 ft. A linearized relationship between the wing and the tail icing severity parameter was used.

2.6 Atmospheric Disturbances

Aircraft icing is assumed to have a unique effect on the performance, stability and control of an aircraft. However, atmospheric disturbances may produce similar changes in aircraft performance and control under some situations. It is important to show that these effects can be distinguished from aircraft icing. Both gravity waves and microburst are studied in this paper to determine their ability to generate icing-like effects.

Microbursts are a well-known atmospheric phenomenon that can degrade aircraft performance and flight safety. Microbursts occur close to the ground and are usually encountered during landing and takeoff operations. In terms of the aircraft, the phenomenon is seen initially as a headwind, then as a downdraft, and finally as a tailwind as seen in Fig. 4.[16] When the aircraft first encounters the headwind it experiences an increase in performance. In order to prevent a climb, the pilot must take action such as reducing power. As the aircraft passes into the downdraft and the tailwind, the performance of the aircraft quickly degrades and can exceed the capabilities of the aircraft to recover from this loss in performance. A microburst model developed by NASA in 1988[17] was used for this analysis. The horizontal and vertical velocities were approximated by the following equations. The u_r and w

velocities in the earth fixed reference frame in cylindrical coordinates were approximated as[17]

$$u_r = \frac{\lambda R^2}{2r}\left[1 - e^{-(r/R)^2}\right]\left(e^{-z/z^*} - e^{-z/\varepsilon}\right)$$

$$w = -\lambda e^{-(r/R)^2}\left[\varepsilon\left(e^{-z/\varepsilon} - 1\right) - z*\left(e^{-z/z^*} - 1\right)\right]$$

Where, r is the distance from the aircraft to the center of the microburst, R is the radius of the downburst shaft, λ is a scaling factor, z is the altitude of the aircraft, z^* is the characteristic height out of the boundary layer, and ε is the characteristic height of the boundary layer. These velocities were converted to rectangular components for use in the FDC analysis.

Gravity waves also present a type of atmospheric disturbance that could potentially resemble the effect of aircraft icing. The type of gravity waves that can affect the aircraft are caused by an air mass being displaced vertically, and then returning to its original locations by gravity or buoyancy. The buoyancy period (time required for an air mass to return to its original position after being displaced) of these waves range from 4 to 7 minutes depending on the altitude in the atmosphere.[18] Although not much information has been collected on these waves, the changes were modeled here as a sinusoidal variation in vertical wind speed.

Implementing these events into the FDC code was straightforward. The FDC had a wind shear model incorporated in the program. This model computes the horizontal components of the wind shear. It then implements the effect of the wind by adding an effective wind component of force along the body fixed axes:[11]

$$F_x = X_{aerodynamic} + X_{propulsion} + X_{gravity} + X_{wind}$$

$$F_y = Y_{aerodynamic} + Y_{propulsion} + Y_{gravity} + Y_{wind}$$

$$F_z = Z_{aerodynamic} + Z_{propulsion} + Z_{gravity} + Z_{wind}$$

where the force components due to the wind are:

$$X_x = -m\left(\dot{u}_w + qw_w - rv_w\right)$$

$$Y_w = -m\left(\dot{v}_w - pw_w + ru_w\right)$$

$$Z_w = -m\left(\dot{w}_w + pv_w - pu_w\right)$$

However, the FDC code does not model the effect of wind gradients, on the scale of the airplane. These wind gradients cause additional roll, pitch, and yaw and are accounted for during microbursts and other atmospheric disturbances.[19] Since this paper's main

concern was the longitudinal system, only the pitch term was added to FDC. The additional term q_g, pitch due to wind gusts or turbulence, was added in the following manner:[19]

$$q_g = -\frac{\partial w_w}{\partial x}$$

Since the FDC turbulence model does not contain a $\partial w_w/\partial x$ term, but contains a $\partial w_w/\partial t$ term, Taylor's Hypotheses[20] was used to approximate $\partial w_w/\partial x$:

$$\frac{\partial w_w}{\partial x} = -\frac{1}{V}\frac{\partial w_w}{\partial t}$$

The additional term was then implemented into the FDC code by adding q_g in the following manner to the already present q term.

$$q_{new} = q - q_g$$

2.7 Verification of Atmospheric Disturbances

The downburst model was verified by comparing an FDC aircraft trajectory to a published twin turboprop trajectory through a downburst.[16] Currently, FDC was not able to make a simulation with the Target Pitch Angle (TPA)[16] escape maneuver, due to limitations in the FDC autopilot program. These limitations are currently being addressed. Therefore, in this study a full-power recovery maneuver was used to simulate the TPA maneuver in FDC. Full power was applied when the microburst was detected based on the detection parameter from reference 16. There were slight differences in the aircraft simulated, although both aircraft were light-twin turboprops. The microburst parameters of both simulations were a radius of 3000 ft, u_{max} of 80 ft/s, and a z_{max} of 150 ft. The initial conditions of both simulations were trimmed flight at an initial altitude of 1400 ft.

It can be seen in Fig. 5 that the simulations were remarkably similar. Differences between the aircraft and flight speeds led to slight differences in the initial angle of attack. The initial jump in the angle of attack on both curves occurs at -2500 ft where the recovery maneuver begins. This is difficult to see on the FDC curve, since the change was very small. After the aircraft passed through the center of the microburst, they both experienced a maximum angle of attack near 3000 ft from the microburst center. In addition, the maximum change in angle of attack was very close to 7 degrees for both aircraft. Both aircraft experienced a

second increase in angle of attack when the recovery maneuver ended. This point occurs much closer to the microburst center for the FDC simulation because of the different flight speed and its effect on the detection parameter. For a preliminary analysis of microbursts for the SIS project this verification was adequate.

3.0 RESULTS AND DISCUSSION

3.1 Effect of Ice Accretion

Through the use of the η and η_{ice} the effect of varying icing cloud conditions on aircraft performance and control can be modeled. The results from the updated iced aircraft model, Fig. 6, are extremely similar to those presented in Bragg et al.[1] The only significant change in the model behavior is presented in Figure 6 a, which shows η versus LWC for 5 different static air temperatures. These plots now show a rapid increase to a definite maximum η value, followed by a very small decrease to an "asymptotic" value. This change is understood by the changes to the g(n) curve described above. The change from a linear g(n) curve to a non-linear g(n) curve explains the non-linear characteristics displayed in Fig. 6 a).

3.2 Neural Net Results

The initial training of the neural networks using all of the available data provided good correlations between the experimental and predicted values. Figure 7 demonstrates the correlation between the predicted neural network lift and drag coefficients (denoted as NN) with the experimental data. The two representative cases shown are the clean case and the case with the horn height of k/c=6.67% located at an s/c=3.4% (horn angle of 60°) with a fully round leading edge. As can be seen in the Fig. 7, the neural network is able to adequately predict the C_l and C_d curves for the clean and iced cases. As mentioned previously, this training of the neural network was only used to determine if a correlation could be found between the ice shape characteristics and the aerodynamic coefficients. Judging from the data presented in Fig. 7, along with the other data not shown, it was determined that a neural network could establish a correlation.

The next step was to create new neural networks trained with only half of the available data. Every other angle of attack point was used. In this way the neural net can be evaluated against data that were not in the training database. The results for all four aerodynamic coefficients from the neural network trained on half of the available data are presented in Fig. 8. The case

shown was the same as shown in Fig. 7, with the horn located at an s/c of 3.4%. The configuration of the network was the same as well, with five hidden layers of ten nodes each. In Fig. 7 the neural net data presented were generated at 0.1° increments to produce many points not in the training data. As can be seen from the figures, training the neural network with only half of the available data had a minimal effect on the network's ability to predict the aerodynamic coefficients.

Figure 8 a) presents the predicted (denoted by NN) and experimental lift coefficients for the clean and iced cases. The predicted values of the network show a good agreement with the experimental data. In addition, the network also adequately captured the reduction in C_{lmax} and α_{max}.

Figure 8 b) shows the predicted and experimental drag coefficients for the iced and clean cases. The correlation was good, with slight deviations at the more negative angles of attack. This was understandable, as most of the experimental data itself were rather anomalous as the angle of attack became more negative. At positive angles of attack, however, the network was able to adequately predict the drag coefficients.

In Fig. 8 c), the moment coefficients for both cases were presented. Overall the correlation was more than acceptable, and the trends were adequately captured.

Finally, Fig. 8 d) demonstrates the correlation between the predicted and experimental hinge-moments. Since the change in the hinge-moment data was subtle with the accretion of ice, the network was able to predict the values of hinge-moment with a high degree of accuracy. More importantly, the network was able to adequately predict the subtle changes, such as the movement of the break point to a lower angle of attack as the ice accretes. Comparisons were also made for the other simulated ice shape sizes and locations with similarly good comparison between the data and the neural net predictions. Research is now underway to expand this to other airfoils and simulated ice accretions.

3.3 Trimmed Flight Characterization

The paper by Bragg et al.[1] showed that the effect and onset of icing on an aircraft can be determined by comparing iced aerodynamic performance values such as velocity, angle of attack and elevator deflection, to the corresponding clean values for similar flight conditions. However, the paper also illustrated the difficulty in resolving wing icing from tail plane icing

using aerodynamic performance values – tail icing resembled a less severe wing icing case.

To distinguish between tail and wing ice, hinge-moment models for the wing and tail surfaces were used. Figure 9 illustrates the results obtained when the aircraft accretes tail ice only, or, wing ice only, by observing the outputs, C_h and $C_{h,RMS}$, obtained from the ailerons and the elevators. Since the aileron deflection used in the FDC code was defined for the right aileron, the aileron hinge-moment measurements were modeled only for the aileron on the right side of the aircraft. For all cases a constant power, constant altitude flight, was maintained by the autopilot feature of the FDC, with the following initial trim conditions:

- Altitude of 7550 ft
- Velocity of 155 knots
- η (t = 0 s) = 0.0

The turbulence was chosen such that the aircraft experienced RMS z-accelerations of 0.15 g. The icing cloud simulated was such that after 600 seconds the ice accretion was represented by $\eta = 0.10$. ($\eta_{ice} = 1.1$).

An analysis of Fig. 9 a) and b) shows that wing ice only and tail ice only can be differentiated by observing both the aileron and elevator hinge-moments. In a wing only ice case, the aileron C_h increased almost two-fold, but the elevator C_h remained almost constant. Similarly, in the tail only ice case, the aileron C_h changed slightly over the 600 second period, but the elevator C_h increased by almost 400%. The change in aileron C_h in the tail ice only case was primarily due to the dependence of C_h on angle of attack, which increased to maintain trim during the iced flight.

Clearly, the hinge-moment measurement, C_h, can be an important input to a method to differentiate between wing ice and tail ice accretion. If there was a significant rise in the aileron hinge-moment, but little change in the elevator hinge-moment, it was probably due to wing only ice. Similarly, if there was an increase in the elevator hinge-moment, but little change in aileron hinge-moment it was probably due to tail only ice. If both the aileron hinge-moment and the elevator hinge-moment increase, it can be inferred that there was ice build-up on both the wing and tail surfaces.

The RMS hinge-moment measurements, $C_{h,RMS}$, displayed similar trends, but were not as effective in detecting ice accretion as the hinge-moment measurement, C_h for the continuous cruise case tested here. This was due to the low angles of attack during the simulations. The $C_{h,RMS}$ increased only at high angles of attack where there was flow separation near the control surfaces. The sudden increase observed in

American Institute of Aeronautics and Astronautics

the $C_{h,RMS}$ was due to the nature of the $C_{h,RMS}$ model illustrated in Fig. 3. An increase in the elevator deflection caused the break in the curve to occur at a lower angle of attack, as did an increase in the icing severity factor, η. As Fig. 9 c) and d) show, noticeable change in $C_{h,RMS}$ occured after a relatively long period of time - more than twice the time it took to notice a similar change in the C_h measurements.

An attempt was also made to characterize the location of ice using hinge-moment measurements and angle of attack at several trim velocities. These scenarios provided the opportunity to detect the location of ice over a wide spectrum of velocity values at a constant icing severity factor. This information could help in determining a suitable approach-to-landing speed for an iced aircraft, thereby avoiding stall. For all cases, a constant altitude flight maintained by the autopilot feature of the FDC was simulated with the following initial trim conditions:

- Altitude of 6560 ft
- $\eta_{ice} = 0.7$

Since a constant altitude flight was chosen, as the trim velocity decreased, the trim angle of attack increased to maintain lift to sustain the aircraft at the specified altitude. The elevator and aileron hinge-moment calculations and angle of attack were obtained at the following trim velocities and resulting angles of attack with wing ice (w_ice) and tail ice (t_ice):

- V = 78 kts ; α = 12.9° (w_ice), 12.5° (t_ice)
- V = 97 kts; α = 6.8° (w_ice), 6.6° (t_ice)
- V = 117 kts; α = 3.4° (w_ice), 3.3° (t_ice)
- V = 136 kts; α = 1.38° (w_ice), 1.38° (t_ice)
- V = 155 kts; α = 0.05° (w_ice), 0.04° (t_ice)

Figure 10 a) and b) show C_h and $C_{h,RMS}$ respectively, as a function of angle of attack for the elevator and aileron in both the wing ice only and clean case. Figure 11 a) and b) show C_h and $C_{h,RMS}$ respectively, as a function of angle of attack for the elevator and aileron in both the tail ice only and clean case.

For the C_h variation as a function of angle of attack in the wing ice only case, as shown in Fig. 10 a), the elevator hinge-moment showed little change between clean and iced conditions as expected, while the aileron hinge-moment showed a modest variation between the clean and iced cases. The $C_{h,RMS}$ variation as a function of angle of attack, Fig. 10 b), showed a drastic increase in the RMS aileron hinge-moment. For the iced case, the $C_{h,RMS}$ rose from 0.005 at an angle of attack of 3.5° to 0.015 at an angle of attack of 7°, and to 0.027 at an angle of attack of 12.5°. There was little change in the

aileron $C_{h,RMS}$ value for the clean case as the airfoil did not approach stall at angles of attack less than 12°. As expected, the elevator $C_{h,RMS}$ showed little change for the wing only iced case.

Similarly, the tail ice only case, Fig. 11, showed the RMS hinge-moment value provided a quicker indication of ice accretion on the tail surface. For the iced case, the $C_{h,RMS}$ rose from 0.005 at an angle of attack of 3.5° to 0.018 at an angle of attack of 6.5°. This jump in values of $C_{h,RMS}$ while comparing the clean condition to the iced condition provided a clear and early indication of the location of ice at angles of attack within the safe flight envelope. The hinge-moment values, C_h, provided reasonable data at low angles of attack and the RMS hinge-moment values, $C_{h,RMS}$, provide excellent warnings of ice build-up at higher angles of attack. The unsteady hinge-moment sensor measurements, $C_{h,RMS}$, provided a good warning of eminent stall and its applicability as an envelope protection tool should be explored.

3.4 Atmospheric DisturbanceAnalysis

In order to compare the effect of microbursts and icing on aircraft performance, flight through 11 different microbursts were simulated using the FDC. The intensity of the microbursts were varied by systematically varying the radius and u_{max}, the maximum outflow of the microburst. For all simulations the aircraft was at 136 kts, and altitudes from 1312 ft to 2625 ft. An altitude hold autopilot setting with no recovery maneuver was used during each microburst simulation in FDC. No recovery maneuver was performed because these simulations were performed under the assumption that the microburst could be mistaken for icing and performing a recovery maneuver indicates that the microburst had been identified. The microburst parameters have been provided in Table 2. Sample wind velocities for microburst #5 have also been provided in Fig. 12.

It was determined that the pitch rate due to wind gust term, q_g term, had little effect on the microburst results. Fig. 13 is an example of the differences between the angle of attack response of the aircraft with and without the q_g term. It can be seen that the results were virtually identical.

The aircraft response to two microburst encounters were compared to three icing encounters and reported in Fig. 14. Angle of attack, velocity, altitude, and elevator angle vs. time can be seen for microbursts #5 and #9 and icing conditions $\eta_{ice} = 0.50$, $\eta_{ice} = 0.91$, and $\eta_{ice} = 1.10$ Figs. 14 a) – d), respectively. All four figures show that the changes in angle of attack,

velocity, altitude, and elevator angle due to icing were very gradual and the changes due to the microbursts were much more rapid and pronounced. In the altitude case, the autopilot was able to maintain altitude during the icing cases while it was not able to maintain altitude during the microbursts. Table 3 summarizes the maximum rates of change for angle of attack, velocity, altitude, and elevator angle for six microbursts and three icing cases. Many of the microburst rates of change were an order of magnitude larger than the icing cases. The rates of change of icing that are similar occur well beyond the time it would take to go through a microburst. By monitoring the rates of change and the altitude it should be possible to distinguish between icing and microbursts. This could be accomplished using a neural net where the change with time can be incorporated.[21]

In addition to mircrobursts, gravity waves could potentially pose a challenge in aircraft ice detection using the SIS. A simple sine wave was used to approximate the downdraft velocity of the gravity waves in the FDC code. The amplitudes and wavelengths of these waves were varied from 0.486 kts. (1 m/s) to 7.7754 kts. (4 m/s) and 1 mile to 15 miles respectively.[18,22] The periods of these wave encounters were set by the aircraft airspeed of 136 kts. Table 4 has been included specifying parameters of the gravity waves analyzed.

The resulting angle of attack, velocity, elevator deflection, altitude, and hinge-moment graphs for the icing and microburst encounters have been included in Figs. 15 a) - f), respectively. In the first 100 seconds the results for icing and the gravity wave cases were similar. This was especially true for the small amplitude and large wavelength waves. The icing simulations shown were for a constant power setting, therefore, as discussed earlier, ice accretion increased drag which caused a reduction in airspeed. As a result of the increase in drag and reduction in airspeed the aircraft increased angle of attack to maintain altitude. Similarly, with the gravity waves, the downdraft forced the aircraft to increase angle of attack to maintain constant altitude. This change in angle of attack caused the aircraft to reduce velocity and make other associated trim changes. Although the mechanisms of both these phenomenon were different, the performance and handling qualities effects were very similar. However, icing also affects the aerodynamics of the aircraft in other ways not duplicated by gravity waves. These include reduction in control power, lift-curve slope, static margin, etc. Exploring these effects should provide avenues to distinguish ice accretion.

Considering the results of the gravity wave analysis, a much more in depth study may be warranted. The sine wave used to approximate the downdraft is simplistic. This must be refined to model more of the diversity of the phenomenon. The mechanisms that cause the changes in aircraft performance and handling qualities need to be studied in more detail. This analysis will identify the differences in such a way that algorithms can be developed to provide good identification. The Neural Network methods used to identify icing can be trained based on these characteristics.

4.0 CONCLUSIONS

A method to study the effect of ice accretion on the flight dynamics of an aircraft has been developed. The method was used to evaluate a method for sensing ice accretion through the change in steady-state aircraft parameters. Conclusions from this study include:

1. The neural net did a good job of fitting the aerodynamic coefficients for the clean and iced airfoil data. This holds promise as a method to replace the η_{ice} method currently in use to model the effect of ice on aircraft parameters.
2. The use of control surface hinge-moment modeling provided a potentially useful tool in determining the location of ice accretion.
3. The unsteady hinge-moment predictions provided excellent information at high angle of attack which suggests their use for envelope protection.
4. The clean aircraft in a microburst experiences performance and control changes significantly different in character from an icing encounter.
5. The simple gravity wave models used in this paper produced aircraft performance and control changes similar to the drag increase-induced changes of an icing encounter. This warrants closer examination to ensure that it can be distinguished from an icing encounter using iced-aircraft characteristics not related to the drag rise.

Research is currently underway to improve the iced aircraft models used in this paper, to examine more closely gravity waves and other atmospheric phenomena so that they can be distinguished from icing effects, and to develop real-time envelope protection methods for iced aircraft.

5.0 ACKNOWLEDGEMENTS

REFERENCES

[1] Bragg, M.B., Hutchison, T., Merret, J., Oltman, R., and Pokhariyal, D., "Effects of Ice Accretion on Aircraft Flight Dynamics," AIAA Paper No. 2000-0360, Reno, NV, Jan. 2000.

[2] Bragg, M.B., "Aircraft Aerodynamic Effects Due To Large-Droplet Ice Accretions," AIAA Paper No. 96-0932, Reno, NV, Jan. 1996.

[3] Shaw, Robert J., Ray G. Sotos, and Frank R. Solano, "An Experimental Study of Airfoil Icing Characteristics," NASA TM 82790, Jan. 1982.

[4] Shin, Jaiwon, and Thomas H. Bond, "Results of an Icing Test n a NACA 0012 Airfoil in the NASA Lewis Icing Research Tunnel," NASA TM 105374, Jan. 1992.

[5] Olsen, William, Robert Shaw, and James Newton, "Ice Shapes and the Resulting Drag Increase for a NACA 0012 Airfoil," NASA TM 83556, Jan. 1984.

[6] Haykin, Simon, "Neural Networks: A Comprehensive Foundation," Prentice Hall, Inc., Upper Saddle River, New Jersey, 1999.

[7] Kim, H.S., and Bragg, M.B., "Effects of Leading-Edge Ice Accretion Geometry on Airfoil Aerodynamics," 17th AIAA Applied Aerodynamics Conference, Norfolk, VA, June 1999.

[8] Ranaudo, R.J., Batterson, J.G., Reehorst, A.L., Bond, T.H. and O'Mara, T.M., "Determination of Longitudinal Aerodynaimc Derivatives Using Flight Data From an Icing Research Aircraft," NASA TM 101427 and AIAA 89-0754, Jan. 1989.

[9] Ratvasky, T.P. and Ranaudo, R.J., "Icing Effects on Aircraft Stability and Control Determined from Flight Data," NASA TM 105977 and AIAA 93-0398, Jan. 1993.

[10] R.J. Ranuado, et.al., "The Measurement of Aircraft Performance and Stability and Control After Flight Through Natural Icing Conditions," AIAA 86-9758, 1986.

[11] Rauw, Marc, "FDC 1.3 – A SIMULINK Toolbox for Flight Dynamics and Control Analysis," 1998.

[12] Miller, R and Ribbens, W., "The Effects of Icing on the Longitudinal Dynamics of an Icing Research Aircraft," AIAA Paper No. 99-0636, Reno, NV, Jan. 1999.

[13] Ratvasky, T.P., Van Zante, J.F., and Riley, J.T., "NASA/FAA Tailplane Icing Program Overview," AIAA Paper No. 99-0370, Reno, NV, Jan. 1999.

[14] Gurbacki, H.M., and Bragg, M.B., " Sensing Aircraft Icing Effects by lap Hinge Moment Measurements", 17th AIAA Applied Aerodynamics Conference, Norfolk, VA, June 1999.

[15] Pokhariyal, D., "Effect of Ice Accretion on Aircraft Performance and Control During Trimmed Flight," M.S. Thesis, University of Illinois, Urbana, IL, Dec. 2000.

[16] Mulgund, S.S., and Stengel, R.F., "Target Pitch Angle for the Microburst Escape Maneuver," *Journal of Aircraft*, Vol. 30, No. 6, Nov.-Dec. 1993.

[17] Oseguera, R.M., and Bowles, R.L., "A simple Analytical 3-Dimensional Downburst Model Based on Boundary Layer Stagnation Flow," NASA TM 1000632.

[18] Sica, R.J., "A Short Primer on Gravity Waves," 1999. http://pcl.physics.uwo.ca/pclhtml/gravitywaves.html.

[19] Etkin B., and Etkin D., "Critical Aspects of Trajectory Prediction: Flight in Non-uniform Wind," AGARDograph No. 301, V. 1, 1990.

[20] Bruun, H. H., "Hot-Wire Anemometry: Principles and Signal Analysis," Oxford, New York 1995.

[21] Melody, J., Pokhariyal, D., Merret, J., Basar, T., Perkins, W., and Bragg, M., "Sensor Integration for Inflight Icing Characterization Using Neural Networks," AIAA paper No. 2001-0542, Jan. 2001.

[22] Politovich, Marcia, Private Communication, December 12, 2000.

Table 1 Non-dimensional Derivatives for Twin Otter in Clean and Iced Configurations.

	C_{Z0}	$C_{Z\alpha}$	C_{Zq}	$C_{Z\delta e}$	C_{X0}	K	C_{m0}	$C_{m\alpha}$	C_{mq}	$C_{m\delta e}$
clean	-0.380	-5.660	-19.970	-0.608	-0.041	0.052	0.008	-1.310	-34.200	-1.740
wing_ice	-0.380	-5.342	-19.700	-0.594	-0.050	0.053	0.008	-1.285	-33.000	-1.709
tail_ice	-0.380	-5.520	-19.700	-0.565	-0.046	0.053	0.008	-1.263	-33.000	-1.593
all iced	-0.380	-5.094	-19.700	-0.550	-0.062	0.057	0.008	-1.180	-33.000	-1.566

	$C_{Y\beta}$	C_{Yp}	C_{Yr}	$C_{Y\delta r}$	$C_{l\beta}$	C_{lp}	C_{lr}	$C_{l\delta a}$	$C_{l\delta r}$	$C_{n\beta}$	C_{np}	C_{nr}	$C_{n\delta r}$	$C_{n\delta a}$
clean	-0.6	-0.2	0.4	0.15	-0.08	-0.5	0.06	-0.15	0.015	0.1	-0.06	-0.18	-0.12	-0.001
all iced	-0.48	-0.2	0.4	0.138	-0.072	-0.45	0.06	-0.135	0.0138	0.08	-0.06	-0.169	-0.11	-0.001

Table 2 Microburst Analysis Parameters.

Microburst Number	Microburst Paramaters			Severity
	R (ft)	Umax (ft/s)	Zmax (ft)	Umax/R (1/s)
1	1000	5	150	0.0050
2	1000	10	150	0.0100
3	1000	20	150	0.0200
4	3000	5	150	0.0017
5	3000	10	150	0.0033
6	3000	20	150	0.0067
7	3000	60	150	0.0200
8	3000	120	150	0.0400
9	5000	10	150	0.0020
10	5000	20	150	0.0040
11	5000	40	150	0.0080

Table 3 Rate of Change Comparison for Icing and Microbursts.

Case	$d\alpha/dt$ (deg/s)	dV/dt (kts/s)	dh/dt (ft/min)	$d\delta_e/dt$ (deg/s)
Microburst 1	0.1718	-0.4505	-466.6	-0.0343
Microburst 2	0.3830	-1.1468	-990.3	-0.0805
Microburst 4	0.0269	-0.2000	-150.0	-0.0143
Microburst 5	0.0472	-0.6000	-150.0	-0.0427
Microburst 6	0.1345	-1.5000	-266.7	-0.0851
Microburst 9	0.0229	-0.2917	-55.5	-0.0203
$\eta_{ice} = 0.50, \eta/\eta_{ice} = 0.08$	0.0040	-0.0323	0.0	0.0039
$\eta_{ice} = 0.91, \eta/\eta_{ice} = 0.09$	0.0204	-0.7951	0.0	-0.0196
$\eta_{ice} = 1.10, \eta/\eta_{ice} = 0.09$	0.1030	-0.2537	-5.0	-0.0943

Table 4 Gravity Wave Parameters.

Downdraft Velocity (kts)				
Wavelength		0.000	0.486	1.944	7.775
miles	meters	Period at an airspeed of 136 kts (sec)			
1	1600	22.86	22.86	22.86	22.86
5	8000	114.29	114.29	114.29	114.29
10	16000	228.57	228.57	228.57	228.57
15	24000	342.86	342.86	342.86	342.86
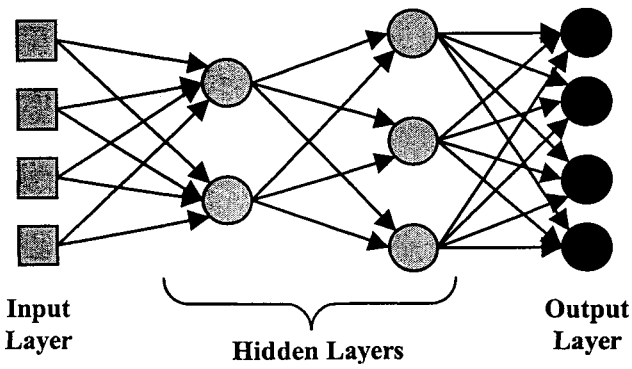
Fig. 1 Schematic of Neural Network.
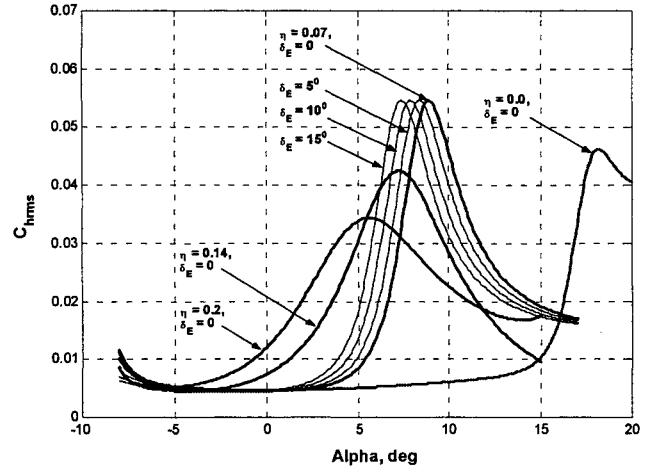
a) $C_{h,RMS}$ model showing variation with α, δ_E and η.
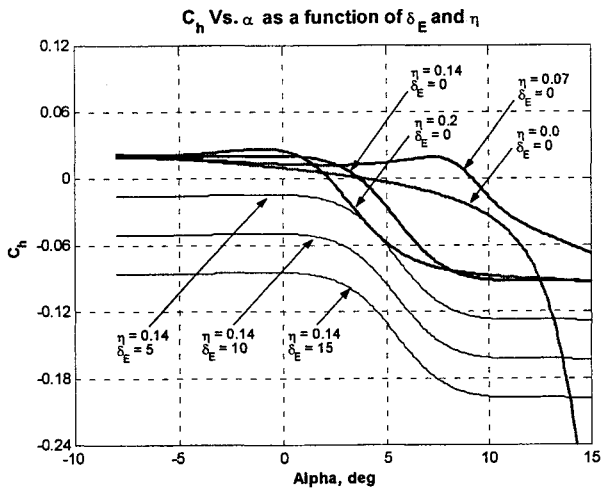
a) C_h model showing variation with α, δ_E and η.
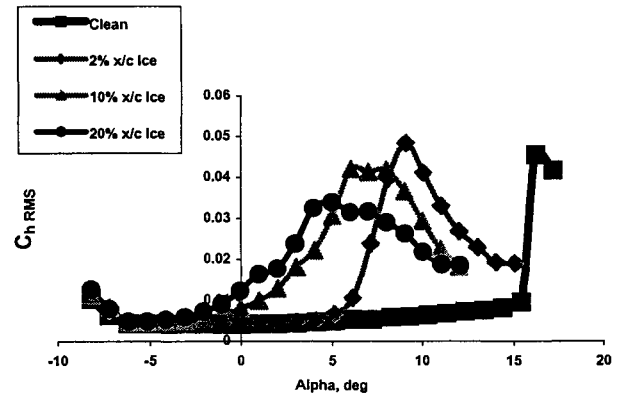
b) Experimental $C_{h,RMS}$ data for NACA 23012 airfoil.

Fig. 3 Unsteady hinge RMS, $C_{h,RMS}$, model compared to experimental data.
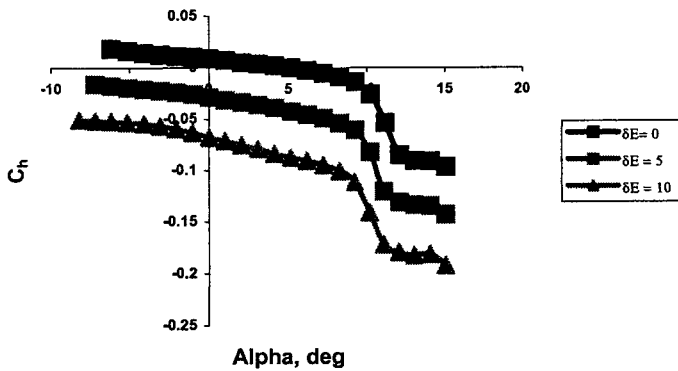
b) Experimental C_h data for NACA 23012 airfoil.

Fig. 2 Hinge moment , C_h, model compared to experimental data.
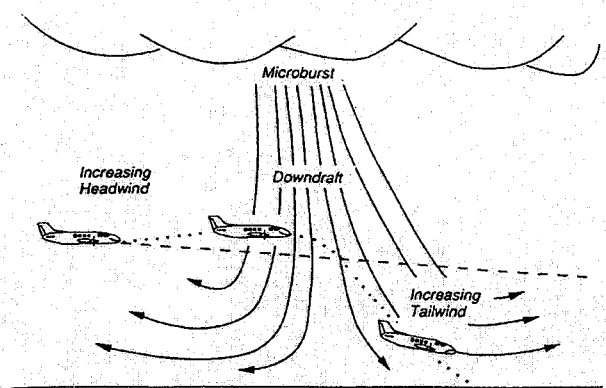
Fig. 4 Microburst Encounter Diagram. [17]
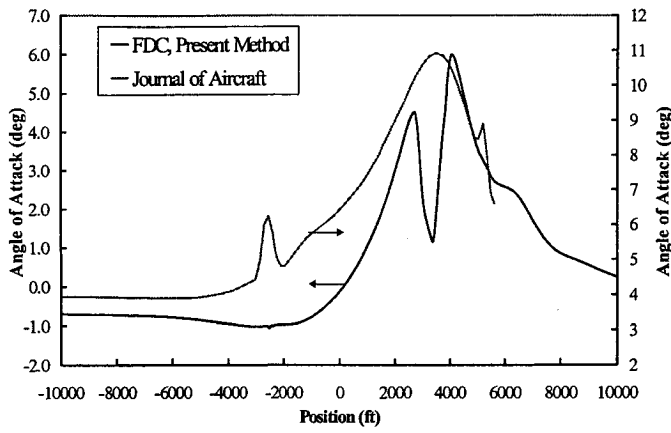
Fig. 5 Verification trajectories. [13]
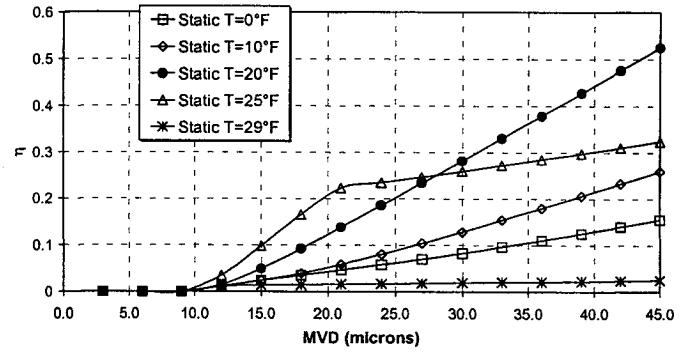
c)   Effect of MVD on η

Fig. 6 Effect of cloud properties on the aircraft icing parameter η.
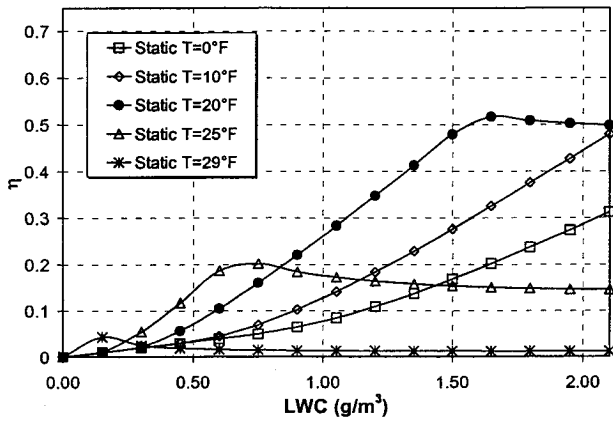
a) Effect of LWC on η.
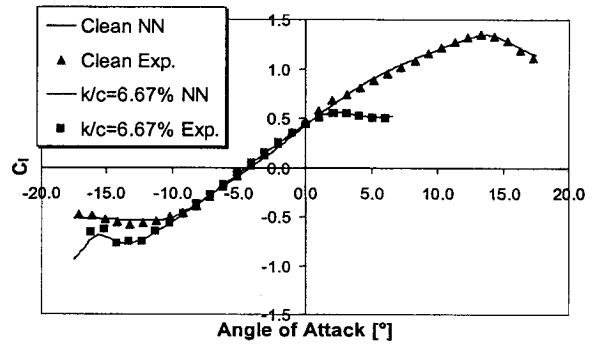
a) Lift Coefficient, C_l.
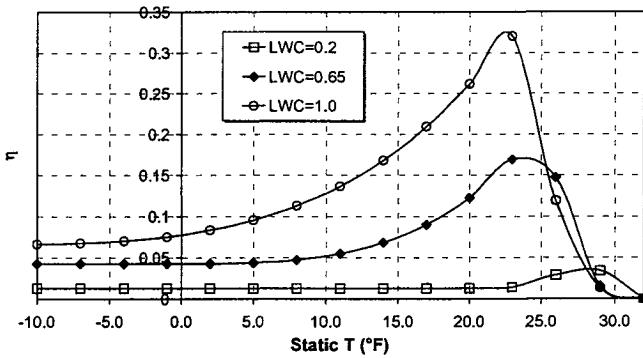
b) Effect of static temperature on η.
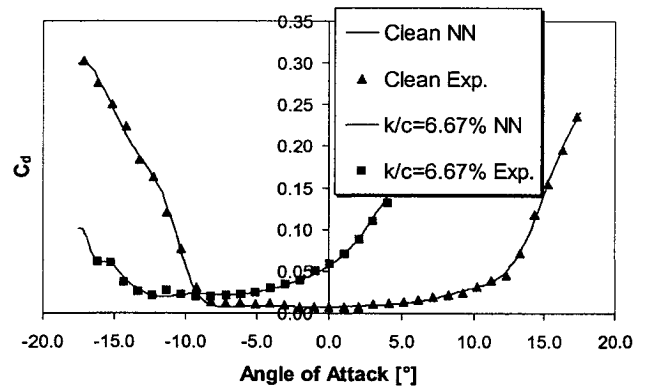
b) Drag Coefficient, C_d.

Fig. 7 Neural net predictions, trained with all data.
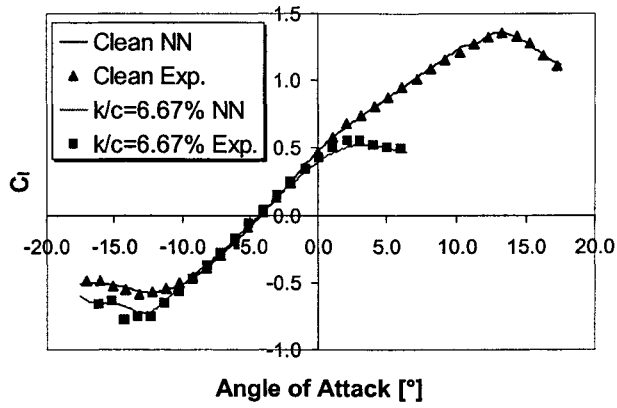
a) Lift Coefficient, C_l.
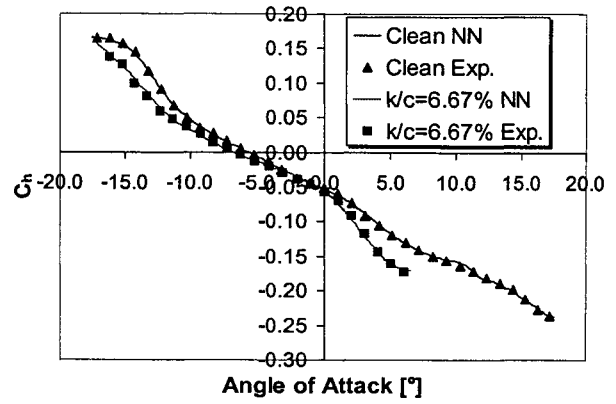
d) Hinge Moment, C_h.

Fig. 8 Neural Net predictions trained with only half of the data.
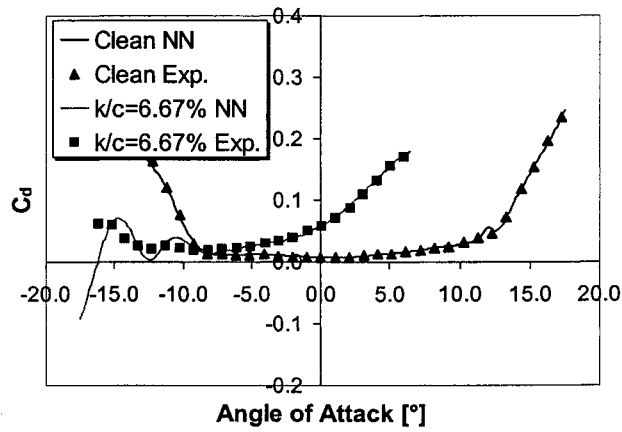
b) Drag Coefficient, C_d.
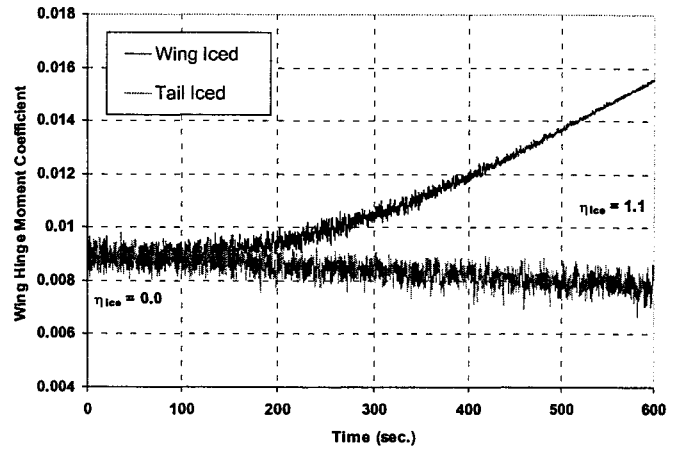
a) Effect of ice location on aileron C_h.
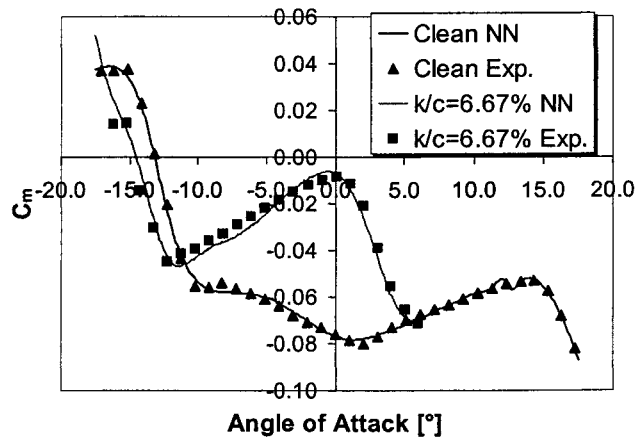
c) Moment Coefficient, C_m.
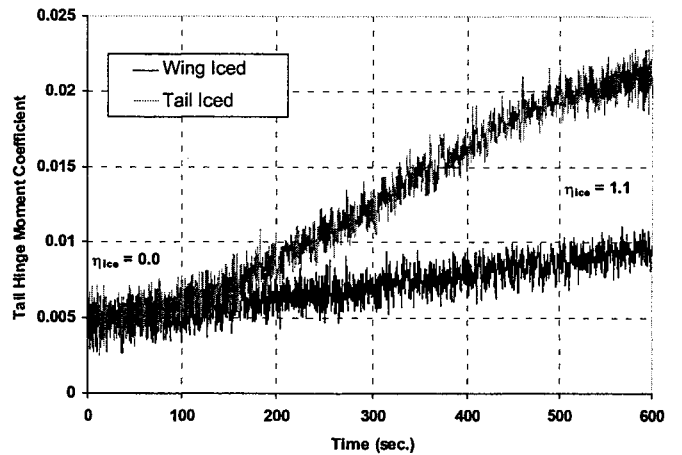
b) Effect of ice location on elevator C_h.
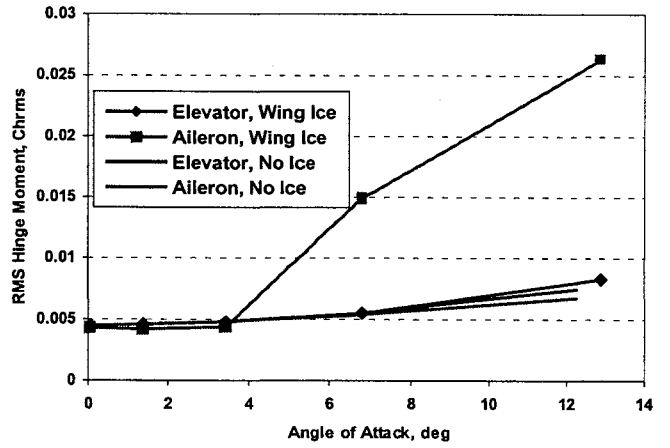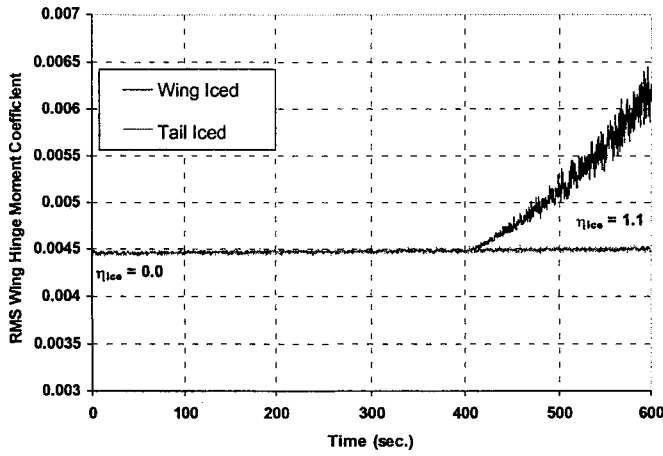
c) Effect of ice location on aileron $C_{h,rms}$.

b) Unsteady hinge moment, $C_{h,rms}$, vs angle of attack.

Fig. 10 Hinge moment values for wing ice only and varying trim velocities.
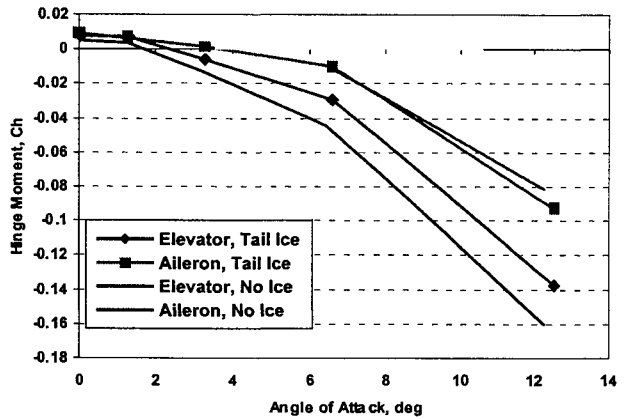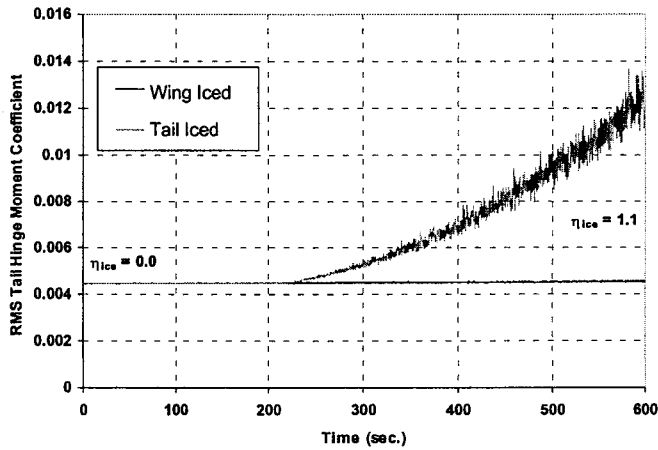
d) Effect of ice location on elevator $C_{h,rms}$.

Fig. 9 Effect of selective icing on hinge moment measurements during cruise flight.

a) Hinge moment, C_h, vs angle of attack.
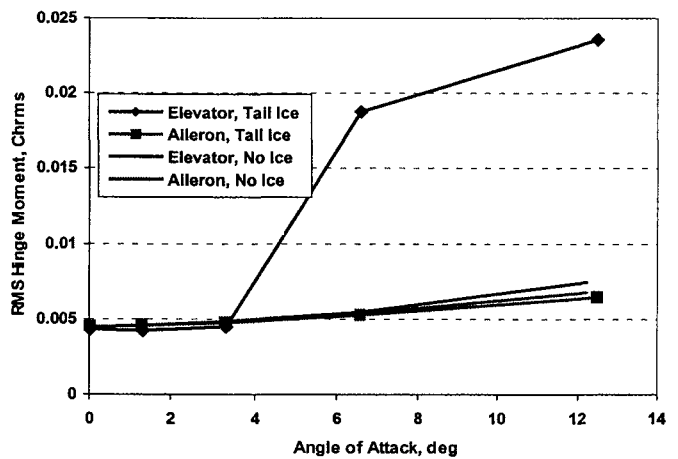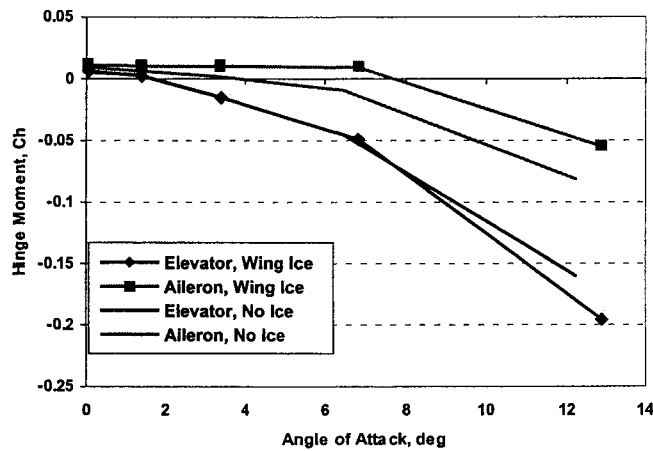
a) Hinge moment, C_h, vs angle of attack.

b) Unsteady hinge moment, $C_{h,rms}$, vs angle of attack.

Fig. 11 Hinge moment values for tail ice only and varying trim velocities.
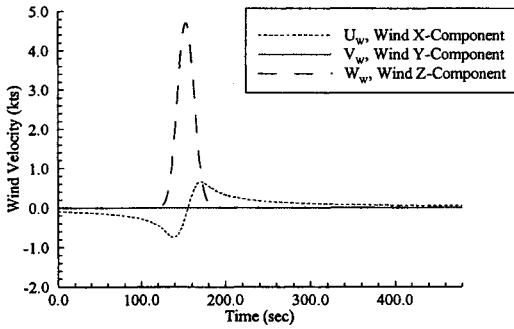
Fig. 12 Sample wind velocities for microburst #5.
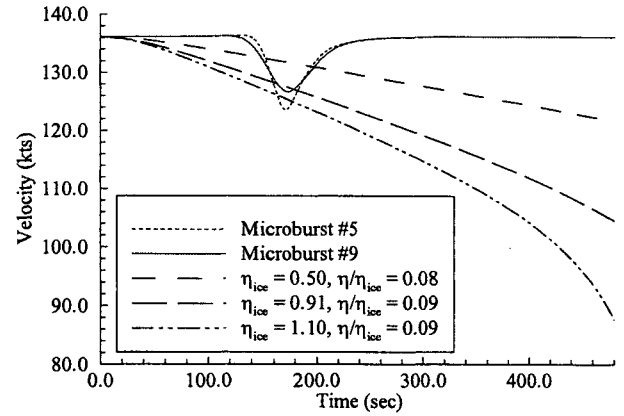
b) Velocity for microbursts and icing.
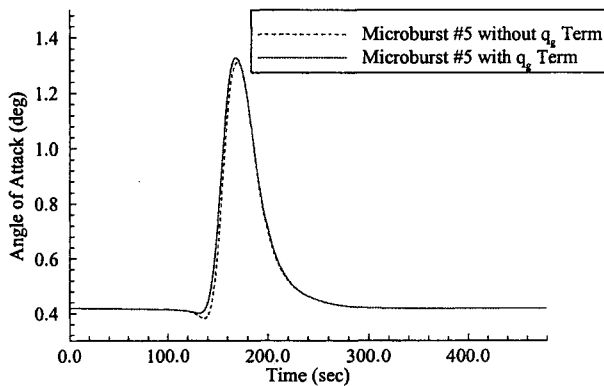
Fig. 13 q_g Effect on the microburst encounter.
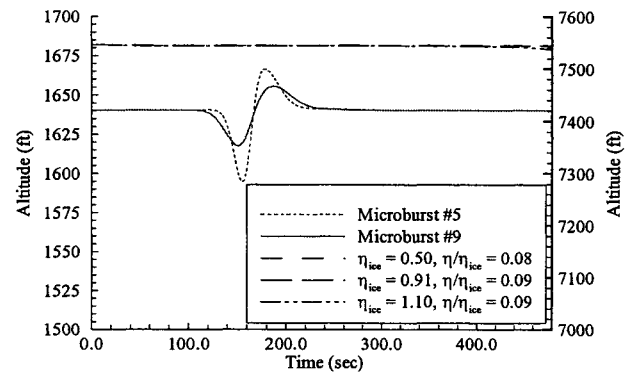
c) Altitude for microbursts and icing.
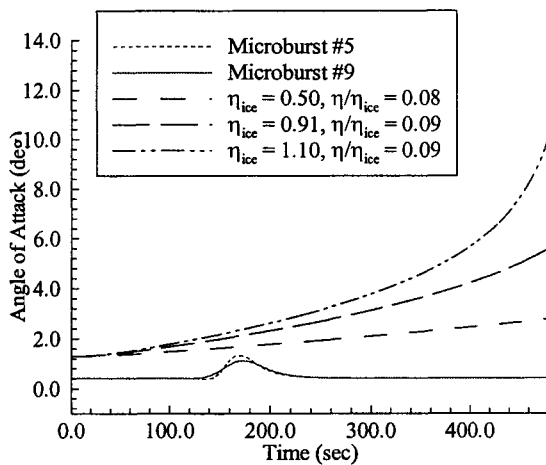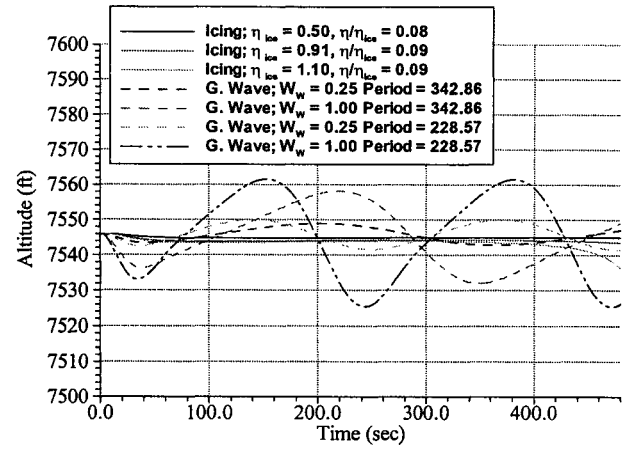

a) Angle of attack for microbursts and icing.
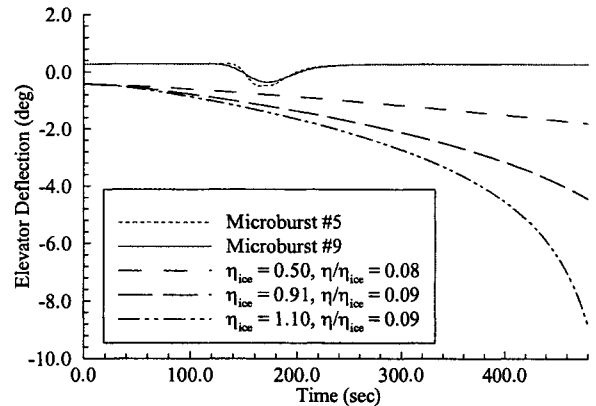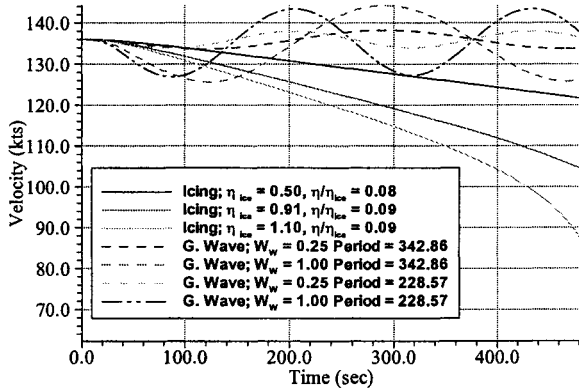

d) δ_e for microbursts and icing.

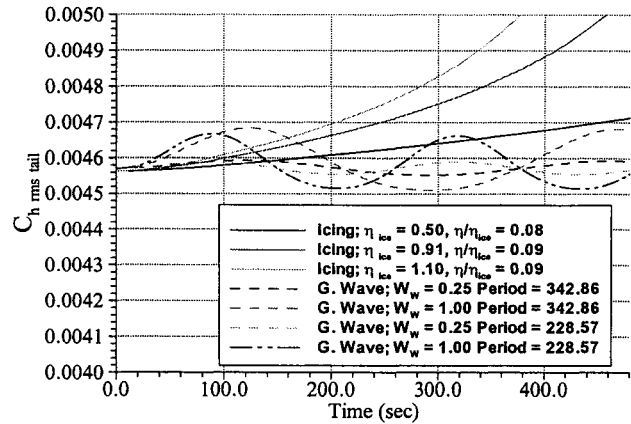Fig. 14 Comparison of the effects of micobursts and icing on aircraft parameters.
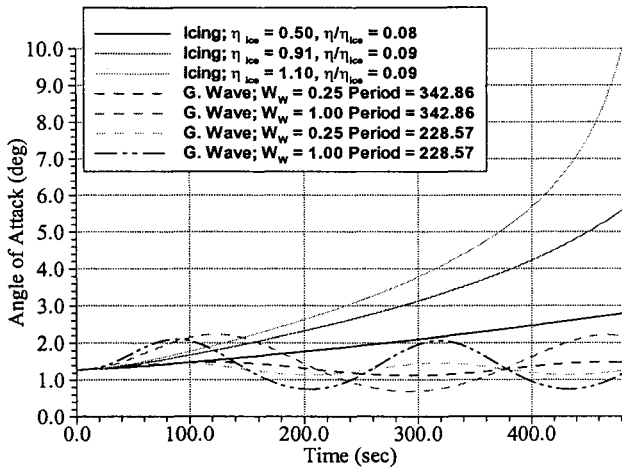
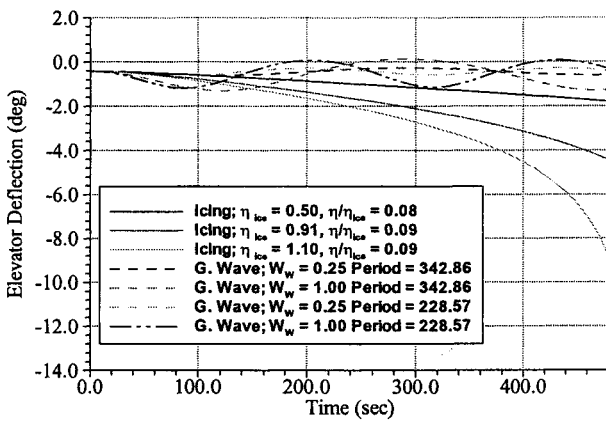a) Angle of attack for icing and gravity waves.
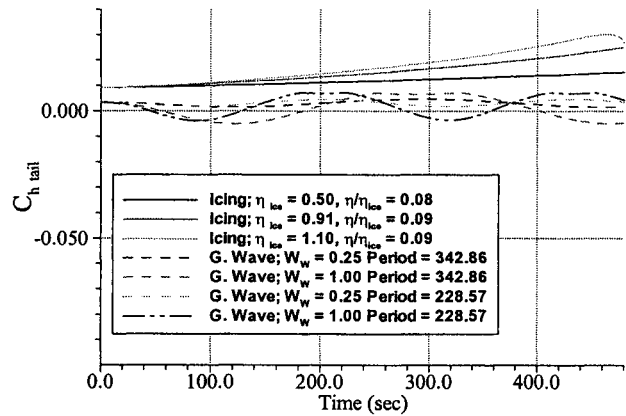

d) Altitude for icing and gravity waves.

b) Velocity for icing and gravity waves.

e) RMS elevator hinge moment coefficient for icing and gravity waves.

c) Elevator deflection for icing and gravity waves.

f) Elevator hinge moment coefficient for icing and gravity waves.

Fig. 15 Comparison of the effects of gravity waves and icing on aircraft parameters.